Inherited Construction of Porous Zinc Hydroxide Sulfate Layer for Stable Dendrite-Free Zn Anodes

Zhicheng Xiang [a], *Yubing Qiu* [a], *Xingpeng Guo* [c], *Kai Qi* *[, a], *Zheng Long Xu* *[, b], and *Bao Yu Xia* *[, a]

[a] School of Chemistry and Chemical Engineering, Key Laboratory of Material Chemistry for Energy Conversion and Storage (Ministry of Education), Hubei Key Laboratory of Material Chemistry and Service Failure, Hubei Engineering Research Center for Biomaterials and Medical Protective Materials, Huazhong University of Science and Technology (HUST), 1037 Luoyu Road, Wuhan 430074, P. R. China

[b] Research Institute of Advanced Manufacturing, Department of Industrial and Systems Engineering, The Hong Kong Polytechnic University, Hung Hom, Kowloon, Hong Kong SAR, China

[c] School of Chemistry and Chemical Engineering, Guangzhou University, Guangzhou, 510006, P. R. China

* Corresponding Author: qikai@hust.edu.cn (K. Qi); zhenglong.xu@polyu.edu.hk (Z. L. Xu); byxia@hust.edu.cn (B. Y. Xia)

Abstract: A stable Zn anode for mitigating dendritic growth, corrosion and byproducts is vital for exhibiting high-performance electrochemical properties in aqueous Zn-ion batteries. An artificial solid/electrolyte interphase is an effective protective strategy for Zn anodes. Herein, a uniform layer of zinc hydroxide sulfate (ZHS) derived *in situ* from a ZIF-8 membrane was developed on a Zn anode. The ZHS layer inherited a well-ordered structure and porous channels from the ZIF-8 membrane and exhibited high ionic conductivity, low electronic conductivity and strong interactions with Zn^{2+}, which facilitated the regulation of homogeneous Zn^{2+} flux and deposition for dendritic inhibition. The strong interaction between H_2O molecules and SO_4^{2-} in the ZHS layer could alter the solvation structure of hydrated Zn^{2+} ions to facilitate the desolvation process, thus mitigating H_2O-induced side reactions during Zn plating/stripping processes. The ZHS layer-coated Zn anode exhibited a remarkably long cycling lifespan of over 2800 h at a low current density of 1 mA cm^{-2} (1 mAh cm^{-2}) and over 1100 h at a high current density of 10 mA cm^{-2} (5 mAh cm^{-2}). This study provides a facile and feasible strategy to achieve interfacial stability of Zn anodes for use in rechargeable aqueous Zn-ion batteries.

Keywords: Zn-ion batteries; Anode corrosion and protection; ZIF-8; Zinc hydroxide sulfate; Desolvation

Introduction

The environmental pollution caused by traditional fossil fuel energy and increasing energy requirements have promoted the in-depth exploration and development of renewable energy, in which Li-ion batteries have dominated the market for rechargeable batteries.[1] Nevertheless, the poor lithium resources, high prices, toxic organic electrolytes and safety hazards of lithium-ion batteries seriously limit their further large-scale application in energy storage.[2] Rechargeable aqueous Zn-ion batteries are promising alternatives owing to their high theoretical gravitational capacity (820 mAh g^{-1}), low electrochemical redox potential (-0.762 V vs. SHE), abundant zinc resources, low cost, environmental friendliness and good safety.[3] However, dendrite formation, corrosion, hydrogen evolution, passivation and byproduct formation are severe challenges for Zn anodes and can reduce the overall performance and service lifespan of zinc-ion batteries. In particular, inhomogeneous Zn deposition could lead to dendritic growth during the Zn plating/stripping process, which would pierce the separators and cause faults in short circuits.[4] The construction of a layer of artificial solid/electrolyte interphase (SEI) is an effective and facile route for stabilizing Zn anodes and can serve as a protective coating to insulate Zn surfaces from aqueous electrolytes, mitigating dendritic growth, corrosion and side reactions.[5]

In recent years, various kinds of artificial coatings or layers have been developed to achieve dendrite-free Zn anodes, such as inorganic coatings (e.g., nanoporous $CaCO_3$ coatings for uniform Zn stripping/plating,[6] a ZrO_2-coated Zn anode for uniform deposition of Zn,[7] a TiO_2 interphase to enhance Zn reversibility[8]), organic polymers (e.g., a polyamide layer for long-life rechargeable Zn anodes,[9] a polyvinyl butyral film functioning as an SEI,[10] poly(2-vinylpyridine) (P2VP)-controlled Zn plating/stripping[11]) and organic−inorganic hybrid composites (e.g., a ZnF_2-enriched interphase for regulated Zn^{2+} flux,[12] an EDTA-grafted MOF interlayer for sustainable Zn anodes,[13] and a UiO-66-COOH coating facilitating dendrite-free

Zn anodes[14]). However, these artificial layers might gradually decompose and detach in electrolytes during Zn plating/stripping cycles, in which the decomposition products would cause unexpected effects on the performance of Zn-ion batteries. In general, the characteristics of ideal SEIs for Zn anodes include but are not limited to low electronic conductivity and high ionic conductivity, which could favor the inhibition of direct reactions between the active Zn surface and aqueous electrolyte, the acceleration of Zn^{2+} transfer kinetics, and the improvement of Coulombic efficiency (CE). The zinc hydroxide sulfate (ZHS) of $Zn_4SO_4(OH)_6{\cdot}xH_2O$ is the typical byproduct of side reactions on Zn anodes during the Zn plating/stripping process,[15] whose inhomogeneous formation would harmfully cause Zn dendritic growth. Notably, ZHS excludes foreign components and is an electrical insulator but ionic conductor; thus, ZHS has high potential to serve as a good candidate for a robust SEI on Zn anodes.[16] However, the general ZHS from the side reactions is distributed sparsely and randomly on the Zn surface rather than as a layer of intact ZHS coating, which cannot effectively protect the Zn anodes. Therefore, constructing an integrated ZHS layer with an ordered structure is a priority for the utilization of ZHS-based SEIs on Zn anodes, which remains a great challenge.

To this end, we propose the use of a homogeneous ZHS layer derived from a ZIF-8 membrane as an artificial SEI on a Zn anode. By a facile method of immersing a Zn plate with a grown ZIF-8 membrane in a $ZnSO_4$ aqueous solution, an integrated ZHS layer composed of $Zn_4SO_4(OH)_6{\cdot}4H_2O$ was generated *in situ* on the Zn surface, which inherited the well-ordered structure and porous channels from the ZIF-8 membrane. The barrier property of the ZHS layer can help to retard hydrogen evolution and corrosion on the Zn surface. Moreover, the ZHS layer intrinsically possesses high ionic conductivity, low electronic conductivity, and strong interactions with Zn^{2+}. These characteristics of the ZHS-based SEI can facilitate the regulation of homogeneous Zn^{2+} flux and deposition to inhibit dendritic growth. The strong interaction between H_2O molecules and the O atoms of SO_4^{2-} in the ZHS layer could alter the solvation structure of hydrated Zn^{2+} ions

and accelerate the desolvation process, mitigating H_2O-induced side reactions and enabling the high reversibility of Zn plating/stripping for stabilizing Zn anodes. The ZHS layer-coated Zn (Zn@ZHS) anode exhibited stable cycling for more than 2800 h at 1 mA cm^{-2} (1 mAh cm^{-2}) and more than 1100 h at 10 mA cm^{-2} (5 mAh cm^{-2}) in symmetric cells. By assembling a Zn@ZHS anode with a MnO_2 cathode, a decent long-term cycling stability with a high average CE of 99.8% was achieved in a full zinc-ion battery.

Results and Discussion

Metal-organic frameworks (MOFs) and their derived nanomaterials possess abundant porous structures, active sites and multiple functional groups; thus, these materials can act as protective layers on the surfaces of Zn anodes and can regulate the chemical characteristics and reaction processes at interfaces to improve interfacial stability.[17] ZIF-8, which is a commonly synthesized MOF with Zn^{2+} centers, is preferentially considered to be an effective functional layer for optimizing the homogeneous diffusion, nucleation and deposition of Zn^{2+}.[18] Herein, a layer of ZIF-8 was prepared on Zn foil (Zn@ZIF-8) by facile solvent thermal synthesis (Experimental Section, Figure S1a-b, Supporting Information, SI), which resulted in a longer cycling lifespan (over 650 h) than that of the bare Zn electrode (only 150 h) at 3 mA cm^{-2} (1 mAh cm^{-2}) in symmetric cells (Figure S1c, SI). After cycling, no ZIF-8 crystals were maintained, and uneven pits could be observed on the electrode surface (Figure S2, SI), which can be attributed to the decomposition of the ZIF-8 crystals. In contrast to the findings of previous studies,[18] it is worth noting that the structure and composition of the ZIF-8 membrane have already undergone certain changes in freshly assembled symmetric cells before charging/discharging. The surface morphologies showed that the ZIF-8 crystals faded away and converted to a porous structure composed of numerous nanosheets (Figure S3, SI). The X-ray diffraction (XRD) patterns clearly match the ZHS peak of $Zn_4SO_4(OH)_6 \cdot 4H_2O$ well (PDF no. 44-0673) (Figure S4, SI). This result

indicates the rapid transformation of ZIF-8 to ZHS in the $ZnSO_4$ electrolyte, which is further verified by the changes in the ZIF-8 powders after soaking in a $ZnSO_4$ aqueous solution (Figure S5-S6, SI). According to previous reports,[19] the mechanism for the transformation of ZIF-8 to ZHS could be speculated as follows: Zn-N bonds are split under the attack of H^+, in which 2-methylimidazole is replaced by SO_4^{2-}, generating intermediates of undisturbed ZIF-8 building blocks; simultaneously, the intermediates react with $Zn(OH)_2$ to transform into ZHS (Figure S7, SI). Thus, what truly works as a protective coating for Zn anodes can be proposed to be the ZIF-8-derived ZHS layer instead of the ZIF-8 membrane. In this case, we systematically explored the ability of the ZIF-8 *in situ*-derived ZHS layer to form a high-performance Zn anode.

Considering the likely incomplete transformation of ZIF-8 to ZHS and the unknown effects of 2-methylimidazole in the few $ZnSO_4$ electrolytes used in the assembled cells, the Zn@ZIF-8 electrodes were soaked in sufficient aqueous solutions of 2 M $ZnSO_4$ for different durations of *in situ* transformation (denoted as Zn@ZHS-*x*, where *x* is the soaking time) before assembling the cells (**Figure 1a**). Scanning electron microscopy (SEM) images showed that the polyhedral ZIF-8 crystals were well-intergrown and formed a homogenous membrane that completely covered the surface of the Zn electrode (**Figure 1b**). After soaking in a $ZnSO_4$ aqueous solution for only 15 s, the surface of Zn@ZHS-15 s exhibited a randomly distributed sheet structure on the ZIF-8 membrane (Figure S8a, SI), whose XRD pattern indicates the hybridization of ZIF-8 and $Zn_4SO_4(OH)_6{\cdot}4H_2O$ (**Figure 1c**). The morphology of Zn@ZHS-3 h shows that no ZIF-8 crystals can be observed, and numerous nanosheets were uniformly constructed into a well-ordered porous structure (**Figure 1d**, Figure S9, SI). The corresponding elemental mapping data indicate that Zn, O and S were homogeneously distributed on Zn@ZHS-3 h without the signal corresponding to N, while only the characteristic peaks of $Zn_4SO_4(OH)_6{\cdot}4H_2O$ can be distinguished in the XRD pattern (**Figure 1c**), suggesting the complete *in situ* transformation of ZIF-8 to ZHS. A thickness of approximately 10 μm and homogeneous distributions of Zn,

O and S were also observed in the cross-sectional SEM image of Zn@ZHS-3 h (**Figure 1e**). The absence of an N signal in the EDS results confirmed the complete transformation of ZIF-8 to ZHS. However, upon increasing the soaking time of Zn@ZIF-8 in the $ZnSO_4$ solution, the compact bulky flakes covered the surfaces of Zn@ZHS-12 h and Zn@ZHS-24 h, whose porous channels were blocked (Figure S8b-c, SI). The XRD patterns indicate the same compositions of $Zn_4SO_4(OH)_6 \cdot 4H_2O$ (**Figure 1c**). The contact angle of Zn@ZHS-3 h (34.7°) was smaller than those of Zn@ZIF-8 (62.6°) and bare Zn (75.7°) (Figure S10, SI). The enhanced hydrophilicity facilitated wetting of the aqueous electrolyte on the surface of Zn@ZHS-3 h, regulating more uniform Zn^{2+} deposition. The 3D morphologies were monitored by atomic force microscopy (AFM), as displayed in **Figure 1f** (Figure S11, SI). The surface of Zn@ZHS-3 h was more even than the relatively rough surface of Zn@ZIF-8, suggesting that the size of the ZHS nanosheets was smaller than that of the ZIF-8 crystals, as determined by the SEM results. The elastic modulus of Zn@ZHS-3 h was determined to be 19.16 GPa by AFM (Figure S12, SI), suggesting that a rigid artificial SEI layer relieves the influence of volume changes during Zn plating/stripping.

The Fourier transform infrared (FT-IR) spectra in **Figure 1g** show that the absorption bands of Zn@ZIF-8 matched well with those of the ZIF-8 powders and were widely divergent from those of Zn@ZHS-3 h. For Zn@ZHS-3 h, the absorption band at 3280 cm^{-1} for the O-H stretching vibration and the characteristic absorption peak of H_2O at 1615 cm^{-1} indicate that Zn@ZHS-3 h contained partial hydrated water. The strong absorption peaks at 1120 cm^{-1} and 598 cm^{-1} are attributed to the bending vibration of SO_4^{2-}, indicating the presence of sulfate ions in Zn@ZHS-3 h. The peaks at 760/1015 cm^{-1} and 515 cm^{-1} are ascribed to the characteristic absorption of Zn-OH and the lattice vibration of Zn-O, respectively.[20] The X-ray photoelectron spectroscopy (XPS) spectra shown in **Figure 1h-i** (Figure S13, SI) further verify the chemical composition of Zn@ZIF-8 and Zn@ZHS-3 h. Compared with that of bare Zn, the N 1 s signal of Zn@ZIF-8 is derived from

the organic ligand 2-methylimidazole in ZIF-8. The disappearance of the N 1 s peak and the appearance of the S 2 s peak for Zn@ZHS-3 h confirm the complete transformation of ZIF-8 to ZHS. The XPS high-resolution Zn 2p spectra of bare Zn include two peaks at binding energies of 1044.8 eV and 1021.8 eV, which are assigned to Zn $2p_{1/2}$ and Zn $2p_{3/2}$, respectively. For Zn@ZIF-8, the peaks at 1045.4 eV and 1022.3 eV could be deconvoluted in the Zn $2p_{1/2}$ and Zn $2p_{3/2}$ spectra, respectively, which are attributed to the Zn-N bond of ZIF-8.[21] The overlapping peaks resolving for Zn@ZHS-3 h could be differentiated at 1045.2 eV and 1022.1 eV, corresponding to the Zn-O (OH^-) bond, and at 1046 eV and 1023 eV, corresponding to the Zn-O (SO_4^{2-}) bond,[22] which are consistent with the composition of $Zn_4SO_4(OH)_6{\cdot}4H_2O$. Time-of-flight secondary ion mass spectrometry (TOF-SIMS) was employed to examine the chemical gradients of Zn@ZHS-3 h, which showed a uniform distribution of S^-, $ZnSOH^-$, and $Zn_4SO_8H_4^-$ species along the sputtering depth (Figure S14, SI). These results demonstrate that the ZIF-8 membrane was completely transformed into a ZHS layer. Both high ionic conductivity and low electronic conductivity are vital features for an ideal SEI on a Zn anode. As shown in **Figure 1j** (Figure S15, SI), the ZHS layer of Zn@ZHS-3 h exhibited an ionic conductivity of 9.70±1.08 $mS{\cdot}cm^{-1}$, which was higher than the 6.30±0.71 $mS{\cdot}cm^{-1}$ for a $ZnSO_4$ electrolyte-infiltrated glass fiber separator (GF), facilitating sufficient Zn^{2+} diffusion for high reversibility of the Zn anode. The electrical resistivity of the ZHS layer was measured to be $9.35\pm0.86 \times 10^3$ Ω·cm, considerably higher than that of the bare Zn surface ($5.50\pm0.12 \times 10^{-6}$ Ω·cm), which could enable the retardation of electron transport to inhibit Zn corrosion and side reactions.

The cycling lifespans of the bare Zn and Zn@ZHS-x electrodes were compared in assembled symmetric cells with a 2 M $ZnSO_4$ aqueous electrolyte. To rapidly screen the stable anodes, **Figure 2a** displays the voltage profiles of the bare Zn-, Zn@ZIF-8- and Zn@ZHS-*x*-based cells at a high current density of 10 mA cm^{-2}

(capacity limited to 5 mAh cm^{-2}) (Figure S16, SI). The bare Zn symmetric cell suffered a short circuit after only 140 h, while the Zn@ZIF-8-based cell exhibited an unstable voltage profile after approximately 310 h. For the Zn@ZHS-*x* anodes, the Zn@ZHS-15 s symmetric cell suddenly short-circuited after approximately 330 h, approaching that of the Zn@ZIF-8 cell, because its principal structure was still the ZIF-8 membrane with only a small quantity of ZHS (Figure S8a, SI). In stark contrast, the Zn@ZHS-3 h symmetric cell exhibited a prolonged cycling lifespan of more than 1100 h. Nevertheless, the short circuit of the Zn@ZHS-12 h symmetric cell suddenly occurred after 510 h of Zn plating/stripping cycles, which could have resulted from blocking the porous structure after a longer transformation time (Figure S8b-c, SI). In addition, the bare Zn foil was soaked in a $ZnSO_4$ aqueous solution as a control. The XRD patterns indicate that the corrosion products were the same as those in the ZHS of $Zn_4SO_4(OH)_6 \cdot 4H_2O$, whose signal appeared on the Zn surface after 2 days of immersion (Figure S17, SI). The SEM images show that many bulky flakes were randomly distributed or stacked on the Zn surface (Figure S18, SI). It can be speculated that the compact bulky flakes on the surfaces of Zn@ZHS-12 h and Zn@ZHS-24 h resulted from the corrosion of Zn substrates under long soaking times. The cycling lifespan of the corroded Zn-based symmetric cell was only 280 h under the same current density and capacity (Figure S19, SI), suggesting the significant role of the ordered porous structure of the ZHS layer. Therefore, owing to having the longest cycling life among all the aforementioned electrodes, the obtained Zn@ZHS-3 h was preferred as the typical specimen for subsequent investigations.

Figure 2b shows that the Zn@ZHS-3 h-based symmetric cell exhibited a low polarization of ≈ 50 mV and a stable voltage cycle of more than 2800 h at 1 mA cm^{-2} (1 mAh cm^{-2}), which boosted the cycling lifespan of the bare Zn electrode by more than 20-fold. When the current density was increased to 3 mA cm^{-2} (1 mAh cm^{-2}), the Zn@ZHS-3 h-cell could still maintain a stable voltage polarization of ≈ 50 mV for more than 2100 h, while the bare Zn cell short-circuited at approximately 160 h (Figure S20, SI). The voltage profiles of the

bare Zn and Zn@ZHS-3 h symmetric cells at different current densities with a limited capacity of 1 mAh cm^{-2} are shown in **Figure 2c**. The Zn@ZHS-3 h-cell exhibited a lower polarization of stable voltage cycles at 1 to 10 mA cm^{-2} than did the bare Zn cell, demonstrating the preferable rate performance of Zn@ZHS-3 h. Zn//Ti and Zn@ZHS-3 h//Ti cells were assembled to measure the CE of Zn plating/stripping at 5 mA cm^{-2} (2 mAh cm^{-2}) to compare the reversibility of the bare Zn and Zn@ZHS-3 h. As shown in **Figure 2d**, the CE of the bare Zn//Ti cell rapidly decreased after only 280 cycles, while the Zn@ZHS-3 h//Ti cell maintained a high average CE of 99.7% over 1500 cycles, reflecting stable Zn plating/stripping circulation. The corresponding voltage profiles of the Zn@ZHS-3 h//Ti cell exhibited lower polarization (≈ 88 mV) than those of the Zn//Ti cell (≈ 109 mV) (Figure S21, SI), verifying the reversible, fast and stable Zn plating/stripping process in the Zn@ZHS-3 h anode.

The cyclic voltammetry (CV) curves indicate that the redox peaks of Zn@ZHS-3 h are close to those of bare Zn, confirming the absence of electrochemical reactions during the Zn plating/stripping process (Figure S22, SI). The peak current of Zn@ZHS-3 h was lower than that of bare Zn, which can be attributed to the relatively higher impedance of the insulating ZHS layer (Figure S23, SI). **Figure 2e** compares the cumulative plated capacity (CPC) of Zn@ZHS-3 h symmetric cells with those of previous reports[6, 14, 17-18, 23], in which our work achieved a high CPC of 5.5 Ah cm^{-2} at 10 mA cm^{-2}, demonstrating the competitive cycling stability of Zn@ZHS-3 h. The feasibility of the Zn@ZHS-3 h anode for practical application in Zn-ion batteries was further evaluated in a full cell using a MnO_2 cathode. **Figure 2f** shows the CV behaviors of the bare Zn//MnO_2 and Zn@ZHS-3 h//MnO_2 full cells. Both CV curves were almost coincident with similar redox peaks and current densities, indicating that the ZHS layer had no negative effect on the electrochemical reactions of the Zn-ion batteries. The rate performances of the full cells based on the bare Zn and Zn@ZHS-3 h anodes are compared in **Figure 2g**. Both full cells delivered almost the same initial specific capacity of ≈ 200 mAh g^{-1} at

a current density of 0.5 C. As the cycle number and current density (1 C, 2 C and 5 C) increased, the specific capacity of the bare Zn//MnO_2 cell decreased more severely than that of the Zn@ZHS-3 h//MnO_2 cell. When the current density was set to 0.5 C, the full cell with the Zn@ZHS-3 h anode recovered well to a specific capacity of ≈ 200 mAh g^{-1}, while the bare Zn//MnO_2 cell only obtained a depressed specific capacity of ≈ 180 mAh g^{-1}. The voltage profiles of the Zn@ZHS-3 h//MnO_2 cell at various current densities revealed two typical plateaus during charge–discharge cycling (Figure S24, SI). Upon increasing the current density from 0.5 C to 5 C, the specific capacity decreased from ≈ 200 mAh g^{-1} to ≈ 130 mAh g^{-1}, corresponding to a capacity retention of 65%. **Figure 2h** compares the charge–discharge curves of the bare Zn//MnO_2 and Zn@ZHS-3 h//MnO_2 cells at a current density of 1C for the 50^{th} cycle and 600^{th} cycle. It can be clearly found that the charge–discharge voltage profiles of the Zn@ZHS-3 h//MnO_2 cell maintained the typical plateaus with a certain reduction in specific capacity after 600 cycles. In contrast, the bare Zn//MnO_2 cell exhibited severely oblique voltage profiles, almost eliminating the entire capacity. The fluctuations in the specific capacity of the full cells during long-term cycling are displayed in **Figure 2i**. A sharp decrease in the specific capacity of the bare Zn//MnO_2 cell was observed after 350 cycles, which decreased to nearly zero after 600 cycles. The Zn@ZHS-3 h//MnO_2 cell maintained a capacity retention above 90% after more than 600 cycles, accompanied by a high CE of 99.8%, indicating decent long-term cycling stability.

To further probe the Zn plating/stripping process, the bare Zn and Zn@ZHS-3 h electrodes were observed *in situ* using a transparent symmetric cell at a plating current density of 1 mA cm^{-2} in a 2 M $ZnSO_4$ electrolyte, whose real-time optical photographs are shown in **Figure 3a**. Visible protrusions appeared on the surface of the bare Zn electrode after 5 min of Zn plating and rapidly grew within 20 min, resulting in potential Zn dendrites with the safety hazard of short circuiting. In comparison, the Zn@ZHS-3 h electrode maintained a

flat surface without obvious dendrites throughout the entire plating process. When the plating current density was 1 mA cm^{-2} (1 mAh cm^{-2}), the protrusions of the deposited Zn agglomeration scattered on the bare Zn surface, while the porous structure of the Zn@ZHS-3 h surface was evenly filled by plated Zn without the appearance of heterogeneous protrusions. After the plating process, both electrodes were applied at a stripping current density of 1 mA cm^{-2} (1 mAh cm^{-2}), whose morphologies are shown in **Figure 3b**. The bare Zn surface showed local corrosion pits due to anodic dissolution, which induced more uneven Zn deposition during the next plating process. In contrast, Zn@ZHS-3 h recovered its well-organized porous structure, demonstrating its superior reversibility for the Zn plating/stripping process. In addition, the morphologies of the bare Zn and Zn@ZHS-3 h electrodes in the cells after cycling were compared *via* optical photographs and SEM images (**Figure 3c**; Figure S25-26, SI). After 100 cycles at 1 mA cm^{-2} (1 mAh cm^{-2}), uneven corrosion was observed on the surface of the bare Zn anode, while both the plated and stripped bare Zn anodes exhibited loose and heterogeneous Zn deposition/dissolution. The XRD pattern further revealed the existence of characteristic peaks corresponding to $Zn_4SO_4(OH)_6 \cdot 4H_2O$ (PDF no. 44-0673) on the bare Zn surface (Figure S27, SI), which should be products of corrosion or side reactions. In comparison, no visible corrosion was detected on the surface of the Zn@ZHS-3 h anode, which maintained the stable structure of the ZIF-8-derived ZHS layer with pore filling/recovery during the Zn plating/stripping process. To verify the ability of the ZHS layer to protect against Zn corrosion, the polarization curves in **Figure 3d** indicate that the corrosion rate of 1.63 mA cm^{-2} for the Zn@ZHS-3 h electrode was lower than that of 3.04 mA cm^{-2} for bare Zn. The hydrogen evolution curves in **Figure 3e** show that the cumulative volume of hydrogen evolution for Zn@ZHS-3 h (≈ 0.17 mL cm^{-2}) was much less than that for bare Zn (≈ 1.13 mL cm^{-2}) during 7 days of immersion in 2 M $ZnSO_4$ aqueous electrolyte. Similarly, the linear sweep voltammetry curves also show that the current density needed for hydrogen evolution on the Zn@ZHS-3 h electrode was lower than that needed for hydrogen evolution on bare Zn (Figure

S28, SI). These results demonstrate that the ZHS layer can retard corrosion and hydrogen evolution on the Zn electrode owing to its intrinsic insulating effect on the barrier properties, which is conducive to obtaining a high average CE for the Zn@ZHS-3 h anode.

Chronopotentiometry and chronoamperometry analyses were performed to investigate the Zn deposition behaviors on the electrodes. **Figure 3f** shows that the nucleation overpotential on the Zn@ZHS-3 h electrode (19.4 mV) was notably lower than that on bare Zn (51.9 mV), which indicated a lower Zn nucleation barrier, facilitating rapid and even Zn deposition. The CV curves of the bare Zn and Zn@ZHS-3 h symmetric cells also displayed a decrease of 25.9 mV in the nucleation overpotential for Zn@ZHS-3 h (Figure S29, SI). As displayed in **Figure 3g**, the current density on bare Zn increased rapidly and continuously under a polarization potential of -150 mV for 400 s, suggesting the rampant and uncontrollable 2D diffusion of Zn^{2+} on the electrode surface for uneven Zn deposition and Zn dendrite risk. After 100 s of potentiostatic polarization on the Zn@ZHS-3 h electrode, the current density reached a constant, indicating steady Zn^{2+} 3D diffusion for homogeneous Zn deposition. The distributions of Zn^{2+} concentration and current density during the Zn plating process were simulated through COMSOL, as shown in **Figure 3h-i**. An uneven distribution and concentration gradient of Zn^{2+} flux appeared on the bare Zn surface, in which the concentrated Zn^{2+} and the larger current density at the nucleation sites revealed local Zn deposition, gradually evolving into dendritic growth. In contrast, a homogeneous Zn^{2+} flux occurred on the surface of the coated Zn, where the concentration of Zn^{2+} at the interface was slightly greater than that in the bulk electrolyte. An evenly distributed current density contributes to uniform and dendritic-free Zn deposition. To thoroughly comprehend the mechanism of the ZHS layer toward the stable Zn anode, the Zn^{2+} affinities of the bare Zn surface and the ZHS layer were compared *via* density functional theory (DFT) calculations. **Figure 3j** shows the models for calculating the interaction between Zn^{2+} and the surfaces of Zn(001) and ZHS(002), which are typical crystal planes of the

Zn surface and ZHS layer, whose binding energies and adsorption distances are shown in **Figure 3k**. The ZHS layer exhibited a greater Zn^{2+} binding energy of -2.74 eV and a shorter Zn^{2+} adsorption distance of 2.33 Å ($d_{Zn\text{-}O}$) than did the bare Zn surface, which had values of -0.62 eV and 2.74 Å ($d_{Zn\text{-}Zn}$), respectively. This means that the ZHS layer has a stronger affinity for Zn^{2+} than does the bare Zn surface, which might be attributed to the strong interaction between Zn^{2+} and the electronegative O atoms of the SO_4^{2-} groups. In this case, the ZHS layer could strongly adsorb and immobilize Zn^{2+} to enable the even distribution of Zn^{2+} flux at the electrode/electrolyte interface, which was confirmed by the adsorption of Zn^{2+} on Zn@ZHS-3 h (Figure 30, SI). This approach would be beneficial for mitigating the growth of Zn dendrites induced by the tip effect.

Moreover, compared with those of the bulk electrolyte, the porous structure and interfacial chemistry of the ZHS layer could induce special solvation behavior in $ZnSO_4$. Raman spectroscopy was used to compare the solvation structures of $ZnSO_4$ in the bulk electrolyte and in the ZHS layer (**Figure 4a**). The Zn^{2+} ions in a typical $ZnSO_4$ aqueous solution exist as the outer solvation structure of the solvent separated ion pair (SSIP), which is $[Zn^{2+}(H_2O)_6]$. The loss of several hydrate H_2O molecules evolves the solvation mode from the SSIP to contact ion pairs (CIPs), such as $[Zn^{2+}(H_2O)_5(SO_4^{2-})]$, in a high-concentration $ZnSO_4$ solution. The peak at ≈ 390 cm^{-1} that represents the vibration of Zn-OH_2 appears for both the SSIP and CIP, which was observed in both the bulk $ZnSO_4$ and the $ZnSO_4$ in the ZHS layer. In comparison, the peak at ≈ 270 cm^{-1} assigned to the Zn-O vibration of $[Zn^{2+}(SO_4^{2-}]$ is a characteristic signal of CIP and was detected only for $ZnSO_4$ in the ZHS layer. Moreover, the ν-SO_4^{2-} band at ≈ 984 cm^{-1} in the spectrum of $ZnSO_4$ in the ZHS layer clearly shifted to a higher frequency than that in the bulk $ZnSO_4$ spectrum (≈ 980 cm^{-1}), which is additional evidence that $[Zn^{2+}(SO_4^{2-})]$ is involved in the evolution of the SSIP to CIP.[24] This means that the ZHS layer could facilitate the desolvation of $[Zn^{2+}(H_2O)_6]$, leading to a new solvent configuration and enabling high reversibility of the

Zn plating/stripping process, while a reduced amount of H_2O molecules would retard corrosion and side reactions on the Zn electrode. In the Zn plating process, the hydrated ions of $[Zn^{2+}(H_2O)_6]$ move toward the anode from the bulk electrolyte, subsequently desolvate with the removal of H_2O molecules and migrate to the Zn surface for nucleation/deposition. The desolvation and migration processes can be evaluated by the thermodynamic property of activation energy (E_a), which is analyzed by electrochemical impedance spectroscopy (EIS) at different temperatures and calculated by the Arrhenius equation (Figure S31, SI).[25] The E_a of the symmetric Zn@ZHS-3 h-cell (32.18 kJ·mol^{-1}) was smaller than that of the cell with the bare Zn anode (42.93 kJ·mol^{-1}), as depicted in **Figure 4b**. Considering that the ZHS layer would partly increase the difficulty of Zn^{2+} migration compared with that of bare Zn, the decreased E_a of Zn@ZHS-3 h demonstrated an easier desolvation process.[26]

To thoroughly probe the desolvation behavior of the ZHS layer, DFT calculations were further performed to analyze the interaction between the $[Zn^{2+}(H_2O)_6]$ and the ZHS layer. The electrostatic potential (ESP) distribution of ZHS was calculated, as shown in **Figure 4c** (Figure S32, SI). This indicates that the O atoms of the SO_4^{2-} groups concentrate the main negative charges, which could serve as interaction sites for Zn^{2+} ions and H_2O molecules by electron-donating action. A comparison of the interactions of Zn^{2+} ions with those of the bare Zn and ZHS layers is displayed in Figures 3j-k, confirming the stronger adsorption of Zn^{2+} by ZHS. Moreover, the interactions of H_2O molecules with Zn and ZHS were calculated and are shown in **Figures 4d-g**. A strong adsorption energy of -0.41 eV corresponded to the interaction of H_2O molecules with the O atoms of SO_4^{2-} in the ZHS layer *via* hydrogen bonds, whereas a weak interaction of -0.35 eV occurred between the bare Zn surface and H_2O molecules without obvious binding sites. The strong interaction between the ZHS layer and H_2O could facilitate desolvation *via* the removal of H_2O molecules from hydrated Zn^{2+} ions, which would contribute to lowering polarization and mitigating H_2O-induced Zn corrosion and hydrogen

evolution.[27]

Figure 4h depicts the desolvation and subsequent migration processes of Zn^{2+} ions in the ZHS layer. First, the hydrated ions of $[Zn^{2+}(H_2O)_6]$ are gradually desolvated to $[Zn^{2+}(H_2O)_{x-1}(SO_4^{2-}\text{-ZHS})]$ (x = 6~1) through the strong interaction of H_2O and O atoms of SO_4^{2-} in ZHS by hydrogen bonds, where DFT calculations were performed to compare the desolvation energies. **Figure 4i** indicates that the stepwise desolvation energies of $[Zn^{2+}(H_2O)_{x-1}(SO_4^{2-}\text{-ZHS})]$ (x = 6~1) were lower than those of $[Zn^{2+}(H_2O)_x]$, indicating easier removal of coordinated H_2O (Figure S33, SI). Moreover, the atomic charges and O-H bond orders were further calculated to compare the structures of $[Zn^{2+}(H_2O)_6]$ and $[Zn^{2+}(H_2O)_5(SO_4^{2-}\text{-ZHS})]$. As displayed in **Figure 4j**, the positive charge of the zinc ion in $[Zn^{2+}(H_2O)_6]$ was +1.07 due to electron donation from the O atoms of H_2O to Zn^{2+}. A lower positive charge of +0.94 for the zinc ion in $[Zn^{2+}(H_2O)_5(SO_4^{2-}\text{-ZHS})]$ revealed the stronger electron-donating ability of (SO_4^{2-}-ZHS). The negative charge of -0.52 for the O atoms of H_2O in $[Zn^{2+}(H_2O)_5(SO_4^{2-}\text{-ZHS})]$ was greater than that of -0.49 in $[Zn^{2+}(H_2O)_6]$, while the bond distance of 2.154 for Zn-OH_2 in $[Zn^{2+}(H_2O)_5(SO_4^{2-}\text{-ZHS})]$ was greater than that of 2.128 in $[Zn^{2+}(H_2O)_6]$. This indicates that (SO_4^{2-}-ZHS) relieves electron donation from H_2O to Zn^{2+}, in accordance with the result of a decreased desolvation energy. The O-H bond order of 0.90 in $[Zn^{2+}(H_2O)_5(SO_4^{2-}\text{-ZHS})]$ was greater than that of 0.86 in $[Zn^{2+}(H_2O)_6]$, while the O-H bond distance of 0.97 in $[Zn^{2+}(H_2O)_5(SO_4^{2-}\text{-ZHS})]$ was shorter than that of 0.98 in $[Zn^{2+}(H_2O)_6]$ (**Figure 4k**). This suggests that the O-H bond of H_2O in $[Zn^{2+}(H_2O)_5(SO_4^{2-}\text{-ZHS})]$ was strengthened, which stabilized H_2O molecules and reduced the reaction activity of hydrogen evolution (Figure S28, SI). Subsequently, the desolvated Zn^{2+} ions migrate to the Zn anode surface along the adjacent SO_4^{2-} groups in the ZHS layer by electrostatic adsorption, which contributes to a greater Zn^{2+} transfer number (0.58) for Zn@ZHS-3 h than for bare Zn (0.41) (Figure S34, SI). The corresponding migration energy barrier was calculated to be 0.70 eV (**Figure 4l**), which is comparable to that of reported fast Zn^{2+}-conductors.[28] Overall,

the Zn plating processes on the bare Zn and Zn@ZHS-3 h electrodes are schematically illustrated in **Figure 4m**. During the cycles of Zn plating/stripping, the unevenly localized nucleation and deposition of Zn induce the growth of Zn dendrites on bare Zn. In contrast, the ZHS layer inherits a well-organized structure and porous channels from the ZIF-8 membrane, which could regulate homogeneous Zn^{2+} flux and deposition and facilitate the desolvation of hydrated Zn^{2+}, effectively inhibiting Zn dendrites and stabilizing Zn anodes.

Conclusions

In summary, this study proposes a layer of zinc hydroxide sulfate (ZHS) as an artificial SEI on a Zn anode for high-performance aqueous Zn-ion batteries. A ZHS layer composed of $Zn_4(OH)_6SO_4 \cdot 4H_2O$ was constructed *in situ* by the facile method of immersing a Zn plate with a grown ZIF-8 membrane into a $ZnSO_4$ aqueous solution. The barrier property of the ZHS layer helped to protect the Zn surface from corrosion and hydrogen evolution. The well-organized structure and porous channels of the ZHS layer were inherited from the ZIF-8 membrane, and combined with its features of low electronic conductivity, high ionic conductivity and strong interaction with Zn^{2+}, the layer could regulate homogeneous Zn^{2+} flux and deposition, inhibiting Zn dendrite growth. Moreover, the strong interaction between H_2O molecules and the O atoms of SO_4^{2-} in the ZHS layer could alter the solvation structure of hydrated Zn^{2+} ions and accelerate the desolvation process, mitigating H_2O-induced side reactions and enabling high reversibility of Zn plating/stripping for stable Zn anodes. In symmetric cells, the ZHS layer-coated Zn (Zn@ZHS) anode exhibited satisfactory stability for more than 2800 h at 1 mA cm^{-2} (1 mAh cm^{-2}) and for more than 1100 h at 10 mA cm^{-2} (5 mAh cm^{-2}). Furthermore, the assembled full Zn-ion battery with a Zn@ZHS anode and a MnO_2 cathode delivered decent long-term cycling stability, accompanied by a high average CE of 99.8%. The use of a ZIF-8-derived ZHS layer as an SEI could shed valuable light on the design of rechargeable aqueous Zn-based energy storage

systems with interfacial stability.

Supporting Information

The experimental methods, supplementary material characterizations and electrochemical measurements used are available in the Supporting Information.

Conflict of interest

The authors declare no competing financial interests.

Acknowledgments

This work is financially supported by the National Natural Science Foundation of China (22325901, 22175068, 22075092 and 21805103), the Fundamental Research Funds for the Central Universities (2018KFYYXJJ121 and 2019KFYXJJS073), the Innovation and Talent Recruitment Base of New Energy Chemistry and Device (B21003), and the Research Committee of The Hong Kong Polytechnic University under project code 1-CD4M. The authors also acknowledge the support of the Analytical and Testing Center of Huazhong University of Science and Technology for the SEM, XRD, XPS and FTIR measurements.

References

[1] H. Zhang, X. Liu, H. Li, I. Hasa, S. Passerini, *Angew. Chem. Int. Ed.* **2021**, 60, 598.
[2] H. S. Hirsh, Y. Li, D. H. Tan, M. Zhang, E. Zhao, Y. S. Meng, *Adv. Energy Mater.* **2020**, 10, 2001274.
[3] a)J. Yang, R. Zhao, Y. Wang, Z. Hu, Y. Wang, A. Zhang, C. Wu, Y. Bai, *Adv. Funct. Mater.* **2023**, 33, 2213510; b)E. Hu, X.-Q. Yang, *Nat. Mater.* **2018**, 17, 480.
[4] J. Hao, B. Li, X. Li, X. Zeng, S. Zhang, F. Yang, S. Liu, D. Li, C. Wu, Z. Guo, *Adv. Mater.* **2020**, 32, 2003021.
[5] a)P. Wang, S. Liang, C. Chen, X. Xie, J. Chen, Z. Liu, Y. Tang, B. Lu, J. Zhou, *Adv. Mater.* **2022**, 34, 2202733; b)J. Zheng, L. A. Archer, *Sci.Adv.* **2021**, 7, eabe0219.
[6] L. Kang, M. Cui, F. Jiang, Y. Gao, H. Luo, J. Liu, W. Liang, C. Zhi, *Adv. Energy Mater.* **2018**, 8, 1801090.
[7] P. Liang, J. Yi, X. Liu, K. Wu, Z. Wang, J. Cui, Y. Liu, Y. Wang, Y. Xia, J. Zhang, *Adv. Funct. Mater.* **2020**, 30, 1908528.
[8] Q. Zhang, J. Luan, X. Huang, Q. Wang, D. Sun, Y. Tang, X. Ji, H. Wang, *Nat. Commun.* **2020**, 11, 3961.
[9] Z. Zhao, J. Zhao, Z. Hu, J. Li, J. Li, Y. Zhang, C. Wang, G. Cui, *Energy Environ. Sci.* **2019**, 12, 1938.
[10] J. Hao, X. Li, S. Zhang, F. Yang, X. Zeng, S. Zhang, G. Bo, C. Wang, Z. Guo, *Adv. Funct. Mater.* **2020**, 30, 2001263.

[11] X. Cai, W. Tian, Z. Zhang, Y. Sun, L. Yang, H. Mu, C. Lian, H. Qiu, *Adv. Mater.* **2024**, 36, 2307727.
[12] D. Xie, Y. Sang, D.-H. Wang, W.-Y. Diao, F.-Y. Tao, C. Liu, J.-W. Wang, H.-Z. Sun, J.-P. Zhang, X.-L. Wu, *Angew. Chem. Int. Ed.* **2023**, 62, e202216934.
[13] R. Zhang, Y. Feng, Y. Ni, B. Zhong, M. Peng, T. Sun, S. Chen, H. Wang, Z. Tao, K. Zhang, *Angew. Chem. Int. Ed.* **2023**, 62, e202304503.
[14] W. Xin, J. Xiao, J. Li, L. Zhang, H. Peng, Z. Yan, Z. Zhu, *Energy Stor. Mater.* **2023**, 56, 76.
[15] a)X. Gao, Y. Dai, C. Zhang, Y. Zhang, W. Zong, W. Zhang, R. Chen, J. Zhu, X. Hu, M. Wang, *Angew. Chem. Int. Ed.* **2023**, 62, e202300608; b)X. Yu, Z. Li, X. Wu, H. Zhang, Q. Zhao, H. Liang, H. Wang, D. Chao, F. Wang, Y. Qiao, H. Zhou, S.-G. Sun, *Joule* **2023**, 7, 1145.
[16] J. Wang, B. Zhang, Z. Cai, R. Zhan, W. Wang, L. Fu, M. Wan, R. Xiao, Y. Ou, L. Wang, J. Jiang, Z. W. Seh, H. Li, Y. Sun, *Sci. Bull.* **2022**, 67, 716.
[17] R. Yuksel, O. Buyukcakir, W. K. Seong, R. S. Ruoff, *Adv. Energy Mater.* **2020**, 10, 1904215.
[18] X. Liu, F. Yang, W. Xu, Y. Zeng, J. He, X. Lu, *Adv. Sci.* **2020**, 7, 2002173.
[19] H. Zhang, M. Zhao, Y. Lin, *Microporous Mesoporous Mater.* **2019**, 279, 201.
[20] A. Chen, C. Zhao, Z. Guo, X. Lu, J. Zhang, N. Liu, Y. Zhang, N. Zhang, *Adv. Funct. Mater.* **2022**, 32, 2203595.
[21] L. He, G. Huang, H. Liu, C. Sang, X. Liu, T. Chen, *Sci.Adv.* **2020**, 6, eaay9751.
[22] B. Liu, X. Yuan, Y. Li, *ACS Energy Lett.* **2023**, 8, 3820.
[23] a)J. L. Yang, J. Li, J. W. Zhao, K. Liu, P. Yang, H. J. Fan, *Adv. Mater.* **2022**, 34, 2202382; b)J. Zhao, Y. Ying, G. Wang, K. Hu, Y. Di Yuan, H. Ye, Z. Liu, J. Y. Lee, D. Zhao, *Energy Stor. Mater.* **2022**, 48, 82; c)X. Chen, W. Li, S. Hu, N. G. Akhmedov, D. Reed, X. Li, X. Liu, *Nano Energy* **2022**, 98, 107269; d)P. Chen, X. Yuan, Y. Xia, Y. Zhang, L. Fu, L. Liu, N. Yu, Q. Huang, B. Wang, X. Hu, *Adv. Sci* **2021**, 8, 2100309; e)R. Zhao, Y. Yang, G. Liu, R. Zhu, J. Huang, Z. Chen, Z. Gao, X. Chen, L. Qie, *Adv. Funct. Mater.* **2021**, 31, 2001867; f)G. Liang, J. Zhu, B. Yan, Q. Li, A. Chen, Z. Chen, X. Wang, B. Xiong, J. Fan, J. Xu, *Energy Environ. Sci.* **2022**, 15, 1086; g)H. Wang, Y. Chen, H. Yu, W. Liu, G. Kuang, L. Mei, Z. Wu, W. Wei, X. Ji, B. Qu, L. Chen, *Adv. Funct. Mater.* **2022**, 32, 2205600; h)Q. Jiao, X. Zhai, Z. Sun, W. Wang, S. Liu, H. Ding, W. Chu, M. Zhou, C. Wu, *Adv. Mater.* **2023**, 35, 2300850.
[24] a)H. Yang, Z. Chang, Y. Qiao, H. Deng, X. Mu, P. He, H. Zhou, *Angew. Chem. Int. Ed.* **2020**, 132, 9463; b)H. Yang, Y. Qiao, Z. Chang, H. Deng, X. Zhu, R. Zhu, Z. Xiong, P. He, H. Zhou, *Adv. Mater.* **2021**, 33, 2102415.
[25] a)P. Lin, J. Cong, J. Li, M. Zhang, P. Lai, J. Zeng, Y. Yang, J. Zhao, *Energy Stor. Mater.* **2022**, 49, 172; b)H. Dong, X. Hu, R. Liu, M. Ouyang, H. He, T. Wang, X. Gao, Y. Dai, W. Zhang, Y. Liu, Y. Zhou, D. J. L. Brett, I. P. Parkin, P. R. Shearing, G. He, *Angew. Chem. Int. Ed.* **2023**, 62, e202311268.
[26] H. Yang, Y. Qiao, Z. Chang, H. Deng, P. He, H. Zhou, *Adv. Mater.* **2020**, 32, 2004240.
[27] L. Miao, Z. Xiao, D. Shi, M. Wu, D. Liu, Y. Li, X. Liu, Y. Sun, S. Zhong, Z. Qian, R. Wang, *Advanced Functional Materials* **2023**, 33, 2306952.
[28] L. Hong, X. Wu, Y.-S. Liu, C. Yu, Y. Liu, K. Sun, C. Shen, W. Huang, Y. Zhou, J.-S. Chen, K.-X. Wang, *Adv. Funct. Mater.* **2023**, 33, 2300952.

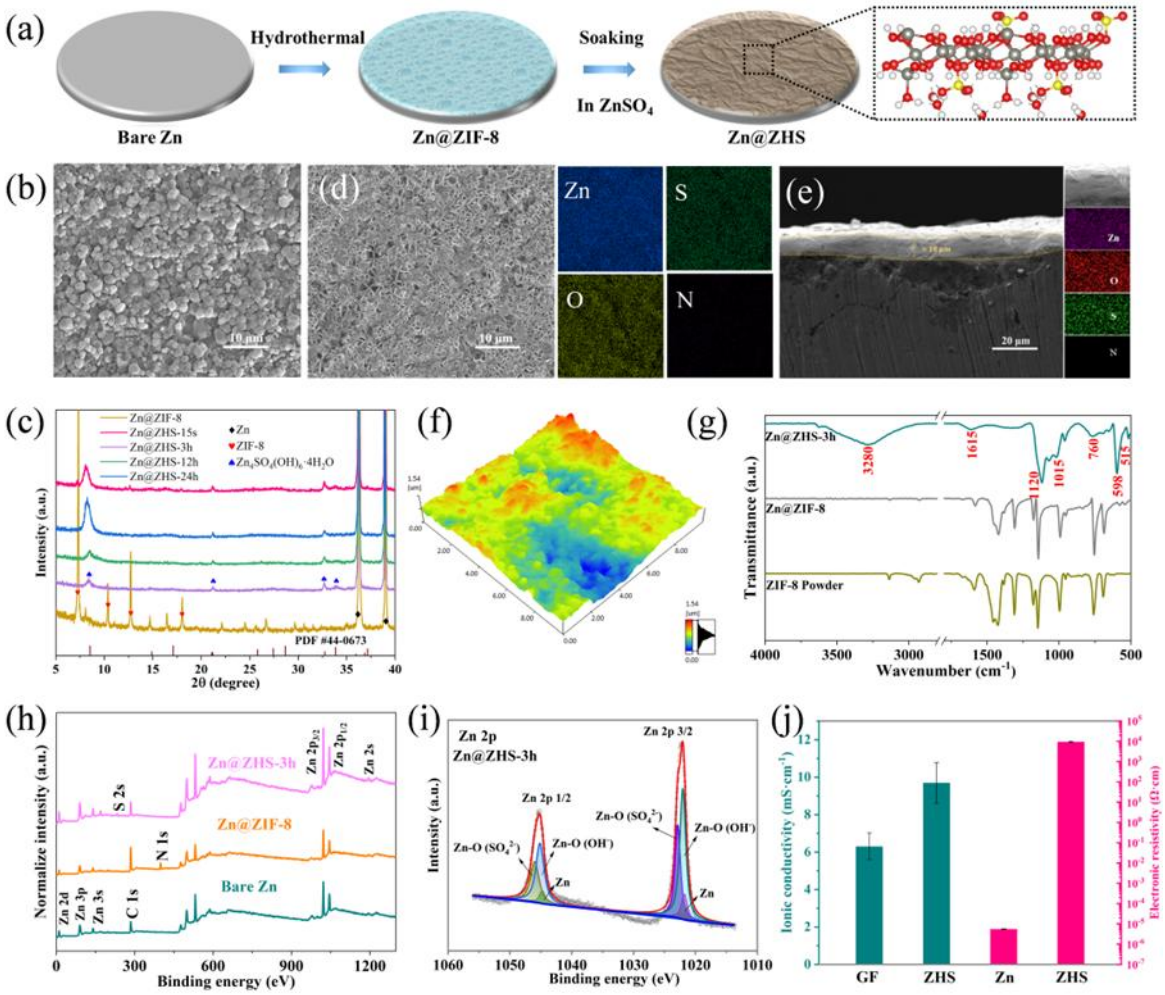

Figure 1. (a) Schematic illustration of the preparation of a ZIF-8-derived ZHS layer on Zn foil. (b) SEM image of Zn@ZIF-8. (c) XRD patterns of different Zn electrodes. (d) Surface and (e) cross-sectional morphologies with corresponding elemental mappings of Zn@ZHS-3 h. (f) AFM 3D morphology of Zn@ZHS-3 h. (g) FTIR spectra of ZIF-8 powder, Zn@ZIF-8 and Zn@ZHS-3 h. (h) XPS survey spectra of different Zn electrodes. (i) XPS high-resolution Zn 2p spectra of Zn@ZHS-3 h. (j) Ionic conductivity of the GF separator and ZHS, as well as the electrical resistivity of Zn and ZHS.

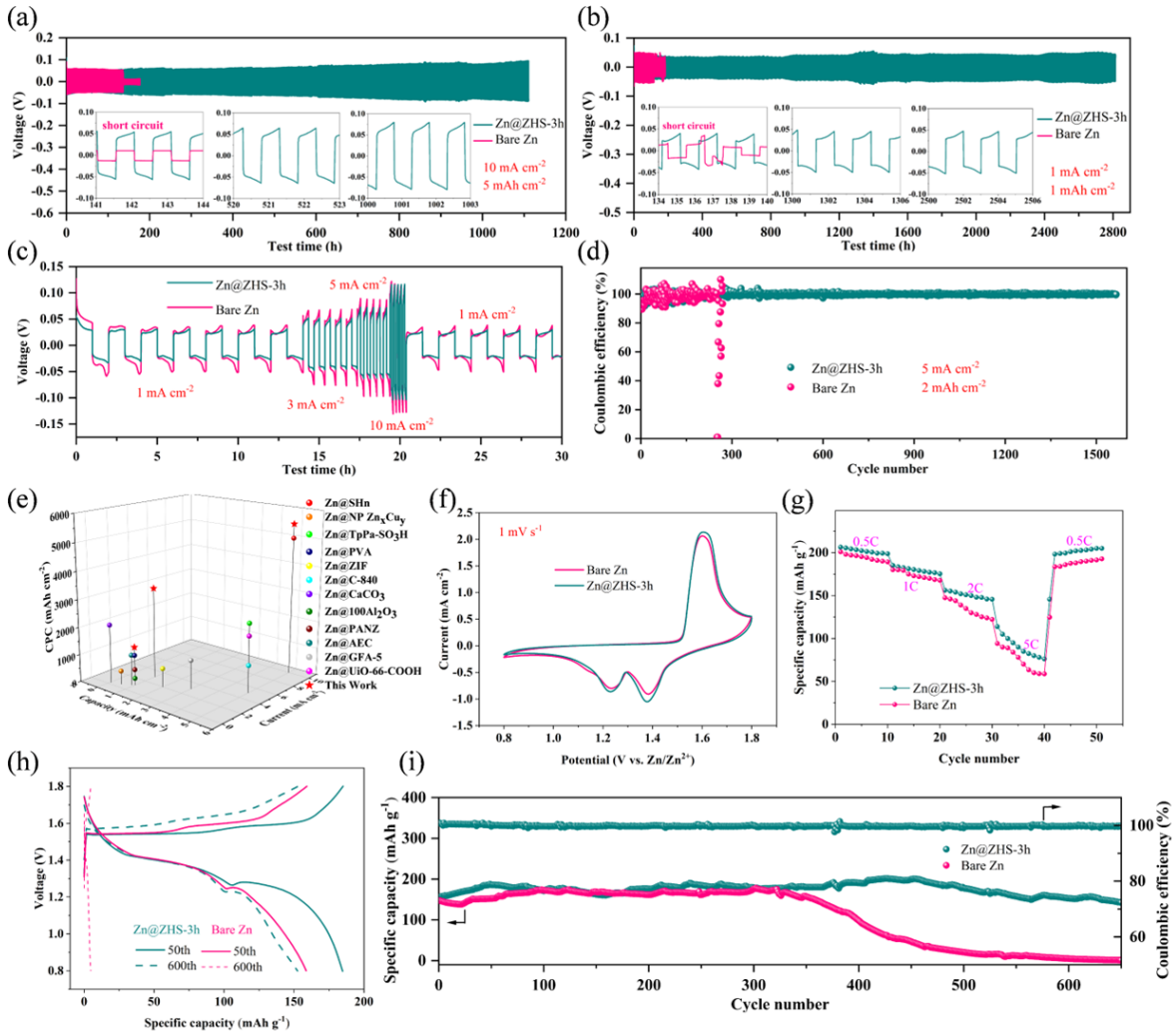

Figure 2. The electrochemical performance of symmetric cells based on bare Zn and Zn@ZHS-3 h: (a, b) Galvanostatic Zn plating/stripping process. (c) Voltage profiles at different current densities with a limited areal capacity of 1 mAh cm^{-2}. (d) Zn plating/stripping CEs of Zn//Ti and Zn@ZHS-3 h//Ti cells. (e) Comparison of the cumulative plated capacity (CPC) with that in previous reports. Electrochemical performance of bare Zn//MnO_2 and Zn@ZHS-3 h//MnO_2 full cells: (f) CV curves at a scan rate of 1 mV s^{-1}. (g) Rate performance at various current densities. (h) Charge–discharge voltage profiles at a current density of 1 C for the 50th cycle and 600th cycle. (i) Long-term cycling stability and CE at a current density of 1C.

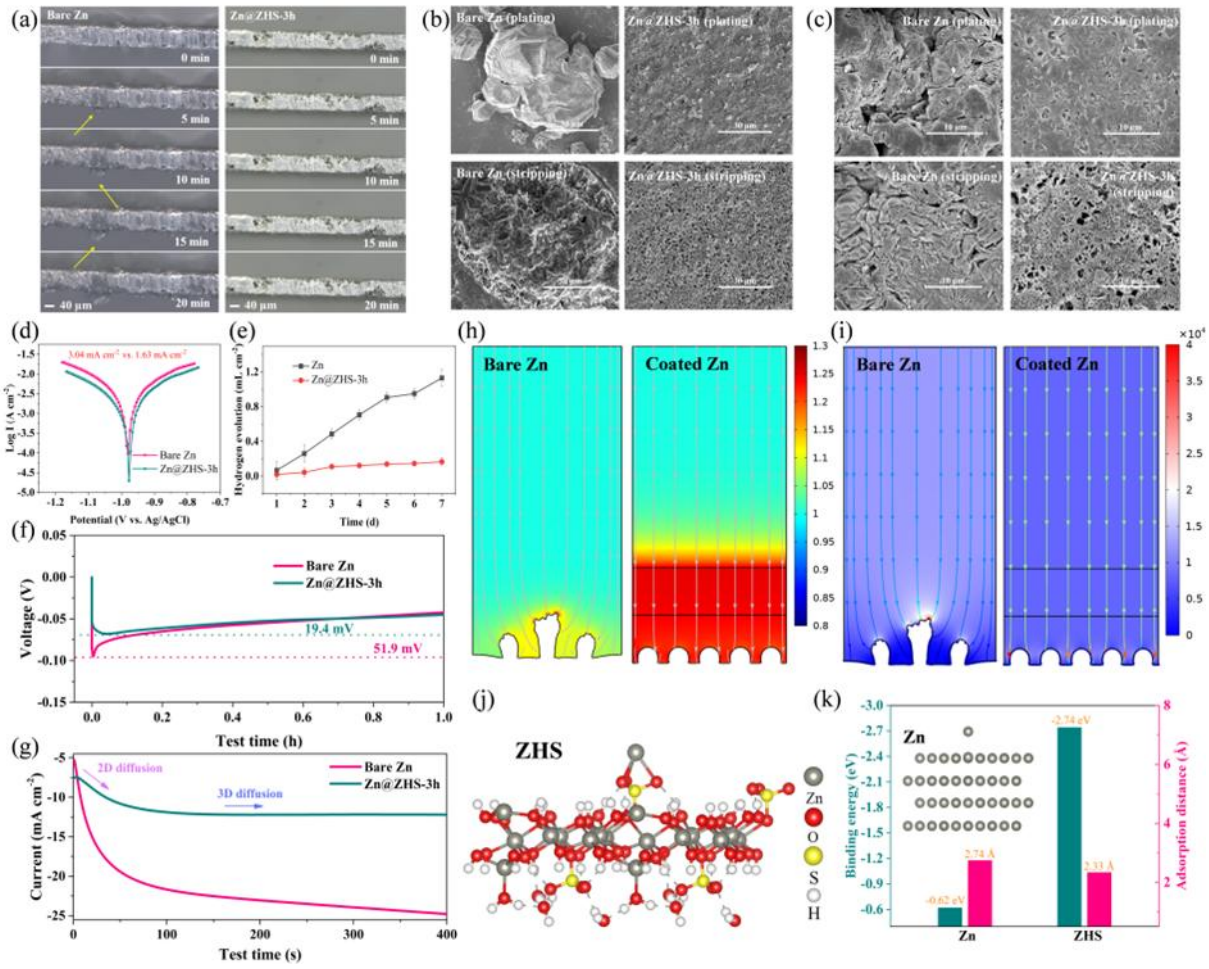

Figure 3. (a) Optical photographs of the *in situ* Zn plating process at 1 mA cm^{-2} on the surfaces of the bare Zn and Zn@ZHS-3 h electrodes. (b) SEM images of Zn plating and stripping processes in the three-electrode system at 1 mA cm^{-2} (1 mAh cm^{-2}) on the surfaces of the bare Zn and Zn@ZHS-3 h electrodes. (c) SEM images of plated and stripped bare Zn and Zn@ZHS-3 h anodes in symmetric cells under a current density of 1 mA cm^{-2} with a capacity of 1 mAh cm^{-2} after 100 cycles. (d) Polarization curves and (e) volumes of hydrogen evolution for bare Zn and Zn@ZHS-3 h in 2 M $ZnSO_4$ aqueous solution. (f) Comparison of the nucleation overpotentials (0.5 mA cm^{-2} for 1 h) and (g) chronoamperometry curves for investigating Zn ion diffusion (-150 mV for 400 s) on bare Zn and Zn@ZHS-3 h in symmetric cells. Distributions of (h) Zn ion concentration and (i) current density on the bare Zn and Zn@ZHS-3 h electrodes. (j) Model for calculating the interaction between Zn^{2+} and the ZHS (002) surface. (k) Binding energy and adsorption distance of Zn^{2+} with respect to the Zn surface and ZHS layer (the inset shows the interaction model between Zn^{2+} and the Zn (001) surface).

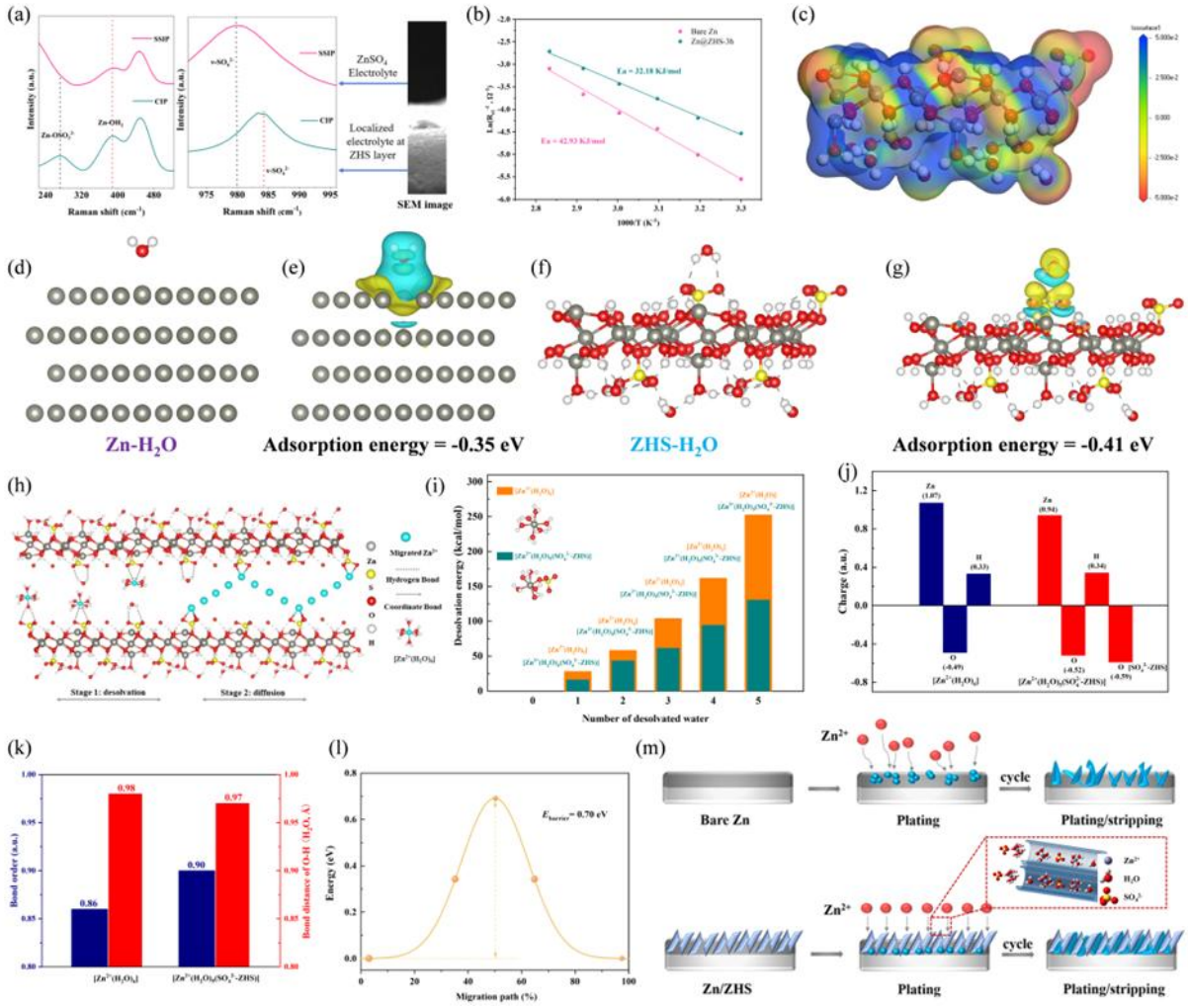

Figure 4. (a) Raman analysis of the $ZnSO_4$ bulk electrolyte and the electrolyte in the ZHS layer. (b) Arrhenius curves and comparison of the activation energies of bare Zn and Zn@ZHS-3 h calculated from Nyquist plots at different temperatures. (c) Electrostatic potential distribution of ZHS (the positive charge is shown in blue, and the negative charge is shown in red). Adsorption configuration and charge density difference of H_2O adsorbed on the (d, e) bare Zn and (f, g) ZHS layers. (h) Desolvation and migration of Zn^{2+} in the channels of the ZHS layer. (i) Desolvation energies, (j) atomic charges, and (k) O-H bond orders and distances of $[Zn^{2+}(H_2O)_6]$ and $[Zn^{2+}(H_2O)_5(SO_4^{2-}\text{-ZHS})]$. (l) Migration energy barrier of Zn^{2+} ions. (m) Schematic illustrations of Zn plating on bare Zn and Zn@ZHS-3 h.